HOKKAIDO UNIVERSITY

Title	In situ synthesis of ordered mesoporous Co-doped TiO2 and its enhanced photocatalytic activity and selectivity for the reduction of CO2
Author(s)	Wang, Tao; Meng, Xianguang; Liu, Guigao; Chang, Kun; Li, Peng; Kang, Qing; Liu, Lequan; Li, Mu; Ouyang, Shuxin; Ye, Jinhua
Citation	Journal of materials chemistry A, 3(18), 9491-9501 https://doi.org/10.1039/c4ta05892e
Issue Date	2015-05-14
Doc URL	http://hdl.handle.net/2115/60969
Type	article (author version)
File Information	Manuscript_J Mater. Chem. A_2014 Ye et al.pdf

Instructions for use

In situ synthesis of ordered mesoporous Co-doped TiO_2 and its enhanced photocatalytic activity and selectivity for the reduction of CO_2

Tao Wang[1], Xianguang Meng[1,2], Guigao Liu[1,2], Kun Chang[1], Peng Li[1], Qing Kang[1], Lequan Liu[1,3], Mu Li[1,2], Shuxin Ouyang[3], and Jinhua Ye[1,2,3]*

[1]*International Center for Materials Nanoarchitectonics (WPI-MANA), and Environmental Remediation Materials Unit, National Institute for Materials Science (NIMS), 1-1 Namiki, Tsukuba, Ibaraki, 305-0044, Japan. Email: Jinhua.YE@nims.go.jp*

[2]*Graduate School of Chemical Science and Engineering, Hokkaido University, Sapporo, 060-0814, Japan*

[3]*TU-NIMS Joint Research Center, School of Material Science and Engineering, Tianjin University, 92 Weijin Road, Tianjin, P.R. China*

Abstract: Ordered mesoporous cobalt-doped titanium dioxide was successfully synthesized by a multicomponent self-assembly process. The doped Co species change the construction of the conduction band and valence band of TiO_2, leading to visible-light absorption for TiO_2. The designed cobalt-doped titanium dioxide performs a higher visible light activity for the reduction of CO_2 among the common reported photocatalysts. In addition, the selectivity of the reduction products is improved by optimizing the energy-band configurations of cobalt-doped titanium dioxide through varying the molar ratio of Co/Ti. When the content of doped cobalt species increases to some extent, Co_3O_4/Co-doped TiO_2 nanocomposites with oxygen vacancies were obtained, which markedly improve the generated rate of CH_4.

Keywords in situ synthesis, cobalt-doped titania, ordered mesoporous structure, cobalt oxide, photoreduction of carbon dioxid

1. Introduction

Reduction of CO_2 is an increasingly important research area because of the fossil fuel shortage and the global warming problem.[1-5] For decades, much effort has been devoted to the development of new technology for the reduction of CO_2, such as biological conversion,[6] thermal catalysis,[7] electrocatalysis,[8-10] artificial photosynthesis,[11, 12]

photo-electrocatalysis[13] and photothermal catalysis.[14, 15] Compared with other technologies, the artificial photosynthesis is still a huge challenge due to the thermodynamic stability of CO_2, and the sluggish formation of renewable hydrocarbon fuels (e.g. CO, CH_4) which is generally less than tens of μmol per hour of illumination per gram of photocatalyst.[11, 12] In artificial photosynthesis, the semiconductor should have appropriate conduction band minimum for the reduction half-reaction and valence band maximum for the oxidation half-reaction. Therefore, the main components of the common photocatalysts for CO_2 conversion are typically wide-band gap semiconductors, such as TiO_2,[16-19] $SrTiO_3$,[20, 21] $NaNbO_3$,[22, 23] Gallate,[24-26] germanate,[27, 28] tantalate,[29] which are photoactivated only under ultraviolet light. Since solar energy is composed of less than 10% of ultraviolet range and the rest are visible and infrared wavelengths, it is necessary to develop a new photocatalyst which has a narrow band gap for the adsorption of visible light and improves the energy conversion efficiency. However, as demonstrated by the extensive researches on photocatalytic reduction of CO_2 with water, the common visible light active photocatalysts, such as oxynitrides,[30, 31] sulfides,[32, 33] phosphide[13, 34-35] and metal-organic frameworks,[36, 37] are quite difficult to promote the oxidation half-reaction, which leads to the generation of oxygen through the oxidation of water.

In recent years, the doping of various cations or anions into wide-band gap semiconductors has been extensively investigated to increase the visible-light adsorption for photocatalytic CO_2 reduction.[38-42] Besides, photocatalysts with ordered

2

mesoporous structures have attracted growing interest due to their uniformly distributed porosity, ordered channels and high specific surface area.[43-45] The highly ordered mesoporous structure develops a high-efficient CO_2 adsorption ability and improves the separation and transport of electron–hole. In addition, the active sites exist not only on the outside surface of mesoporous catalyst, but also exist on the inner surface of pores. Therefore, ordered mesoporous semiconductors with doping of ions have enormous potential for promoting CO_2 reduction under visible light region. Up to now, there are few researches report the doped semiconductor with ordered mesoporous structure for photocatalytic reactions.

Herein, we employ a doping method to adjust the band structure of TiO_2 to promote the absorption of light in visible range and enhance the catalytic ability for oxidation half-reaction. Cobalt-based materials were discovered to be efficient catalysts for water oxidation at relatively low overpotentials,[46-48] and even were able to carry out overall water splitting.[49] Thus, in this paper, ordered mesoporous Co-doped TiO_2 was elaborately prepared by a multicomponent self-assembly process. The prepared ordered mesoporous Co-doped TiO_2 exhibited a much higher photocatalytic activity of CO_2 reduction under visible light owing to their regular porous structure and suitable band structure.

2. Experimental section

2.1 Synthesis of ordered mesoporous Co-doped TiO_2: In a typical preparation, 2.0 g of triblock copolymer Pluronic F127 and a certain amount of cobalt acetate were poured

into 20.0 mL of anhydrous ethanol with vigorous stirring at 40 ^{o}C to obtain a clear solution. Then, 3.4 g of tetrabutyl titanate and 2.5 g of soluble resol were added with vigorous stirring for 2 h at 40 ^{o}C to obtain a homogeneous green solution. After evaporating the solvents at room temperature and thermo-polymerizing in an oven at 100 ^{o}C for 24 h, the resulting green film was pyrolyzed in a tubular furnace at 350 ^{o}C for 4 h under N_2 atmosphere with a heating rate of 1 ^{o}C min^{-1} to get puce polymer-Co-TiO$_2$ composite. Finally, the puce composite was calcined at 400 ^{o}C for 5 h under air atmosphere to obtain ordered mesoporous Co-doped TiO$_2$. The samples were named as Co-OMT-x, where the corresponding molar ratios of Co/Ti in the synthetic process were shown in Table 1. When the addition of cobalt acetate is 0 g, the sample is named as OMT. The mesoporous Co$_3$O$_4$ was prepared by the same procedure, in which the amounts of cobalt acetate and tetrabutyl titanate were 2.49 and 0 g, respectively. The soluble resol (phenol-formaldehyde, Mw < 500, 20 wt% in ethanol) was synthesized according to the method reported by Dr. Zhao.[50]

2.2 Characterization: X-ray diffraction (XRD) patterns were tested on an X-ray diffractometer (Rint 2000, Altima III, Rigaku Co. Japan,) using a Cu Kα source. Nitrogen adsorption-desorption isotherms were measured at 77 K using a BEL SORP-mini II (BEL Japan INC., Japan). The specific surface areas of the samples were calculated by utilizing the Brunauer-Emmett-Teller (BET) method, and the pore size distributions were estimated by the Barret-Hoyner-Halenda (BJH) method by using the adsorption branch. Transmission electron microscopy (TEM) experiments were

conducted by a field-emission transmission electron microscope (2100F, JEOL Co., Japan) operated at 200 kV. Energy dispersive X-ray spectrum (EDX) installed in a 2100F was used to analyze the microzone composition (STEM-EDX mapping). The scanning electron microscopy (SEM) images were recorded on a field-emission-scanning electron microscope (S4800, Hitachi Co., Japan) with an accelerating voltage of 10 kV. The diffuse reflection spectra were measured in an ultraviolet-visible (UV-vis) recording spectrophotometer (UV-2600, Shimadzu Co., Japan) and were transformed to the absorption spectra according to the Kubelka-Munk equation. Element chemical analysis and valence band of the samples were performed by X-ray photoelectron spectroscopy (XPS, PHI Quantera SXM, ULVAC-PHI Inc., Japan). TG/DTA were monitored by using a DTG-60H instrument (Shimadzu Co., Japan) from 25-800 ^{o}C under nitrogen or air with a heating rate of 1 ^{o}C min^{-1}. The oxygen vacancies of the samples were investigated by ESR (Electron Spin Resonance) using JEOL JES-FA-200 at 25 ^{o}C.

2.3 Photocatalytic measurements: All of the samples were treated at 400 ^{o}C in air for 4 h to remove organic adsorbates before the photocatalytic reaction. The photoreduction of CO_2 was carried out in an airtight circulation system. A 300 W Xenon arc lamp with a L-42 glass filter was used as the light source. 0.1 g of the sample was uniformly dispersed on a porous quartzose film in the reaction cell, and 3 mL of the deionized H_2O and 80 kPa pure CO_2 gas were added into the airtight system. The products were measured by using a gas chromatograph (GC-14B, Shimadzu Co., Japan). The isotope

analysis of ^{13}C was analyzed by using a gas chromatohraph-mass spectrum (JEOL-GCQMS, JMS-K9 and 6890N Network GC system, Agilent Technologies).

2.4 Photoelectrochemical and electrochemical measurements: Photoelectrochemical and electrochemical measurements were carried in a quartzose beaker and an electrochemical station (ALS/CH model 650A) using three-electrode mode with a coated ITO as the working electrode, a platinum foil as the counter electrode, and Ag/AgCl electrode as the reference electrode in 0.5 M Na_2SO_4 aqueous solution. For working electrodes, 5 mg of photocatalyst and 10 μL of Nafion solution (5 wt%) were dispersed in 1 mL of ethanol to form a homogeneous turbid liquid and then 50 μL of turbid liquid was deposited on ITO conductive glass with an area of 1 cm^2. Photocurrent densities were measured at 0.4 V (vs. Ag/AgCl), and an AM 1.5 Solar simulator (PEC-L01, Pecell Co., Japan) with an L–42 glass filter as the light source. Mott–Schottky plots were obtained under direct current potential polarization with a potential step of 10 mV at a frequency of 1 kHz.

2.5 Theoretical calculations. Electronic structures of TiO_2 and Co-doped TiO_2 were investigated via the plane-wave-based density functional theory (DFT) using a standard Cambridge serial total energy package (CASTEP) code,[52] then the electronic exchange-correlation energy was analyzed within the frame-work of the local density approximation (LDA).

3. Results and discussion

3.1 Synthesis and characterization of ordered mesoporous Co-doped TiO_2

Fig. 1a describes the designed schematic route for in situ fabricating ordered mesoporous Co-doped TiO_2. Firstly, the triblock copolymer F127 used as a template, phenolic resol precursor act as a "binder" and metal salts co-assembled into rod-like micelles in ethanolic solution. The obtained green solution was poured into petri dish to evaporate the solvent and polymerized at 100 ^{o}C. Secondly, the dark green film was pyrolyzed at 350 ^{o}C under N_2 atmosphere to remove the template (Fig. S1a), and a puce polymer-Co-TiO_2 composite was obtained. Finally, well-crystallized Co-doped ordered mesoporous TiO_2 (Fig. 1(b,c)) was successfully synthesized by getting rid of "binder" through calcining the puce polymer-Co-TiO_2 composite at 400 ^{o}C in air (Fig. S1b). Due to the ionic radius of Co^{2+} and Ti^{4+} are 65 and 60.5 pm,[52] the Co atom can take the place of Ti atom.[53,54] In general, Co-doped TiO_2 was prepared by conventional solid reaction by mixing the TiO_2 with CoO_x or Co salts, which need a high calcined temperature in air. However, when the synthesis of Co-doped TiO_2 was carried out through mixing the Co^{2+} and Ti^{4+} in atomic scale, it only needs a low calcined temperature (~350 ^{o}C) in air.[53,55] when the synthesis of Co-doped TiO_2 was carried out through mixing the Co^{2+} and Ti^{4+} in atomic scale, with a calcined temperature is 400 ^{o}C in air.

As shown in the elemental mapping images (Fig. 1d), the cobalt species are homogeneously doped throughout the TiO_2 framework, thus Co-doped ordered mesoporous TiO_2 is obtained. However, when the molar ratio of Co/Ti reaches to specific value (For example, Co/Ti = 0.2 in Co-OMT-7), lots of nanoparticles with a

diameter of 5–10 nm appear in the mesoporous structure, which are further proved to be cobalt oxides by the TEM image (Fig. 1e,f), elemental mapping images (Fig. 1g), STEM image (Fig. 1h), and the followed XRD analysis. The detailed discussion will be provided in the following parts. As a result, cobalt oxides/cobalt-doped ordered mesoporous TiO_2 composites are prepared in the case of excess addition of cobalt species. As shown in Fig. 1i, series of Co-doped ordered mesoporous TiO_2 with different colors are prepared by varying the mass ratio of cobalt source to titanium source during self-assembly process. The products are denoted as Co-OMT-x (x = 1~8), where the corresponding molar ratio of Co/Ti in the synthetic process is detailed illustrated in the Table 1. What is more, in order to obtain the doping levels of Co^{2+}, we have removed the Co_3O_4 by using HCl treatment, as shown in Fig. S2. The molar ratios of Co/Ti in each samples before and after removing the Co_3O_4 are summarized in Table S1

The morphologies and porous structures of the samples were directly observed by TEM and FE-SEM. As shown in Fig. 1b, Fig. 2, and Fig. S3, when the molar ratio of Co/Ti is lower than 0.05, the corresponding samples (OMT and Co-OMT-x (x=1~5)) present a well-ordered mesoporous structure with pore size of 2–4 nm. Nevertheless, the nanoparticles gradually appear and grow along with the increased addition of cobalt precursors, leading to the collapse of ordered mesoporous structure. The crystal lattice of the nanoparticles embedded in Co-OMT-8 are estimated to be 0.243 nm (shown in Fig. 2h), which corresponds to the crystalline Co_3O_4 (311) facet. For comparison, the

8

Co_3O_4 sample is prepared through a same process except the addition of Ti source. The TEM images in Fig. S4 revealed that Co_3O_4 sample is composed of nanoparticles with the size of 20-40 nm and the interplanar distances of Co_3O_4 (111) and (311) facets are respectively proved to be 0.468 and 0.243 nm by high resolution TEM images (Fig. S4c, d), which is in accordance with that of nanoparticles in Co-OMT-8.

The impacts of doped amount of cobalt on the structures of the obtained samples were investigated by XRD and N_2 adsorption-desorption isotherms. The small-angle XRD patterns for the all of the samples are shown in Fig. 3A. It's observable that pure OMT exhibit an unambiguous diffraction peak at two theta of 1.0°, indicating the ordered mesoporous structure. Whereas, the Co_3O_4 sample presents no diffraction peak, implying that it does not possess ordered porous structure. In the case of Co-doped TiO_2, the intensity of the well-resolved diffraction peaks at around 1.0° gradually decreases along with the increasingly doped amount of Co, suggesting the deterioration of long-range ordered porous structure in TiO_2. In the wide-angle XRD range (Fig. 3B), we can see that all Co-doped TiO_2 samples present anatase (JCPDS Card 21-1272), and the cubic Co_3O_4 phase (JCPDS Card 01-1152) started appearing in Co-OMT-x (x=6,7,8) when the molar ratio of Co/Ti exceeds 0.05. The electric state of Co in Co-OMT-x was investigated by X-ray photoelectron spectroscopy (XPS). The high resolution Co $2p$ spectra in OMT, Co-OMT-x and Co_3O_4 are shown in Fig. S5. As the doped amount of cobalt increases, the characteristic peaks of Co $2p$ are gradually enhanced. Thereinto,

two characteristic peaks with respect to $2p_{3/2}$ and $2p_{1/2}$ confirm the Co^{2+} state in Co-doped TiO_2 materials.[56-58]

N_2 adsorption−desorption isotherms give us more detailed structural information of the samples. As shown in Fig. 4A, Co-OMT-x and OMT samples exhibit type IV isotherms and type H1 hysteresis loops according to the IUPAC classification, generated from the capillary condensation in mesopores.[59] As the amount of cobalt increases, the pore size distribution of Co-OMT-x becomes wider due to the structural destruction (Fig. 4B). When we did not add the Ti salt, the obtained Co_3O_4 shows a non-porous structure. The specific structural parameters of the samples are concluded in Table 1. We can find that the surface areas and the pore volumes of Co-OMT-x trend to decline along with the increase of cobalt because of the deteriorated mesoporous structure, which is in accordance with the small-angle XRD result (Fig. 3A). Generally, the higher specific surface area, the more active sites.[43]

UV-visible absorption spectra of the samples are shown in Fig. 5a,b. All of the samples except pure TiO_2, possess the optical absorption capability in the region of visible light. Moreover, with the gradual increase of Co, the absorption edges displayed a continuous red-shift, implying the narrowing of their band gaps. In the light of the corresponding Tauc plots (Fig. S6), their band gaps are shown in the Table 2. The result suggests that the band gaps of these samples can be tailored by changing the molar ratio of Co/Ti. Furthermore, the photoelectrochemical (PEC) test (Fig. 5c) was carried out to prove the photocurrent response of the samples under visible light. The photocurrent

densities of Co-doped TiO_2 (0.3~0.4 $\mu A \ cm^{-2}$) are much higher than that of pure TiO_2 (0.04 $\mu A \ cm^{-2}$).

3.2 Photocatalytic reduction of CO_2 over ordered mesoporous Co-doped TiO_2

In order to evaluate the impact of cobalt content and porous structure of the samples for CO_2 photoreduction under visible light, we carried out the photocatalytic reaction in a gas-closed circulation system in the presence of water vapor and CO_2. The basic schematic of photocatalytic process over Co-doped TiO_2 is illustrated in Fig. 6a. Generally, in the gas–solid system, CH_4, CO or other organic products and H_2 are the main reduction products, O_2 is the main oxidation product.[54,60,61] According to the previous research, the ordered porous structure and high specific surface area are beneficial to improve the stability and activity of the catalysts.[43] Based on the small-angle XRD (Fig. 3A), N_2 adsorption-desorption isotherms analysis (Fig. 4A) and UV-vis spectra (Fig. 5a,b), we concluded that the structural ordering, specific surface areas and pore volumes of Co-OMT-x trend to decline along with the increased doping of cobalt, but the band gap also decreases to adsorbing more light. Thus, after carefully adjusting and controlling the structure and components in Co-doped TiO_2 by changing the molar ratio of Co/Ti, we can successfully find out the best ratio for CO_2 photoreduction. As shown in Fig. 6b,c, the pure order mesoporous TiO_2 were not able to reduce CO_2 under visible light, and the activities of Co-OMT-x (x=1~5) for CO_2 reduction rises firstly, then decreases along with the increased content of doped cobalt. The best catalyst is Co-OMT-4, in which the theoretical molar ratio of Co/Ti is 0.025.

As demonstrated by TEM (Fig. 2) and XRD (Fig. 3B), the Co species are doped into the TiO$_2$ frameworks when the molar ratio of Co/Ti was controlled less than 0.1 in Co-OMT-x (x=1~5) samples. In this case, we infer that ordered mesoporous structure and band gap are the dominant factors contribute to activity and stability. When the ratio of Co/Ti exceeds 0.1, Co$_3$O$_4$ nanoparticles appear in Co-OMT-x (x=6~8) samples. It is observable from Fig. 6d,e that the evolution rate of CO decreases as the cobalt continues to increase in Co-OMT-x (x=6~8), whereas the evolution rate of CH$_4$ is significantly enhanced. Nevertheless, according to the previous analysis, the structural ordering of Co-OMT-8 is worse than Co-OMT-7 and Co-OMT-4, leading to the poorer stability (Fig. S7). In this situation, the dispersed Co$_3$O$_4$ nanoparticle in ordered mesoporous framework is prevailing reason for activity and stability, and the best theoretical molar ratio of Co/Ti is 0.15.

The H$_2$ and especially O$_2$ are detected in the productions, and the evolution rates of different products are presented in Table 2. It is noteworthy that the photocatalytic performance shown in this study under visible light is significantly higher or comparable in comparison with the previously reported photocatalytic systems under visible light, even under UV-vis light (Table S2).[21,27,43,62-70] However, due to the different experimental conditions (such as light intensity, illumination area, photocatalysts dosage) in these photocatalytic systems, the direct comparison is not appropriate. Therefore, we also compared our materials with some typical semiconductors or composites (including N-doped TiO$_2$, Au/TiO$_2$, C$_3$N$_4$, WO$_3$, P25)

measured in the same reactor system. The experimental details, characteristics and performances of these materials are shown in supporting information (Fig. S8 and Table S2). We can see that the ordered mesoporous Co-doped TiO_2 materials show the optimal photocatalytic activity for CO_2 reduction under visible light (Fig. 6f). In addition, the major products under UV-vis light are also CO and CH_4 for Co-OMT-4, and the corresponding photocatalytic activity (Table S2) is higher than that of pure ordered mesoporous TiO_2.[43] In this study, the porous structure properties and energy-band configurations in the ordered mesoporous Co-doped TiO_2 material can be easily adjusted by tuning the molar ratio of Co/Ti, thus, superior photocatalytic performance can be optimized successfully. Co-OMT-4 shows the best photocatalytic activity, which is 0.09 $\mu mol\ g^{-1}\ h^{-1}$ (CH_4) and 1.94 $\mu mol\ g^{-1}\ h^{-1}$ (CO). The corresponding quantum efficiency of Co-OMT-4 for the photoreduction is 0.031%. Combined Co-doped TiO_2 with Co_3O_4, we can enhance the selectivity of products, and Co-OMT-8 shows the best activity, which is 0.258 $\mu mol\ g^{-1}\ h^{-1}$ (CH_4).

A necessary investigation was performed to confirm whether the products were from CO_2 by using $^{13}CO_2$. As shown in the GC-MS spectrum (Fig. S9a), the peak with the retention time 02:07 is confirmed to be the main product ^{13}CO (named as M) for Co-OMT-4. The intensity ratio of M^+ and $(M-13)^+$ of ^{13}CO (m/z = 29, 16) matches that of ^{12}CO (m/z = 28, 16). In the case of Co-OMT-7 (Fig. S9b), the base peak with the retention time 02:20 is determined to be the parent peak of $^{13}CH_4$ (named as M′). The intensity ratio of M'^+, $(M'-1)^+$ and $(M'-2)^+$ of $^{13}CH_4$ (m/z = 17, 16, 15) matches that of

$^{12}CH_4$ (m/z = 16, 15, 14). Therefore, the main organic product ^{13}CO or $^{13}CH_4$ is verified to be generated from the reduction of $^{13}CO_2$.

As we all know, the electronic structure of a semiconductor plays an important role in the level of the conduction band and the valence band, which subsequently influence the photocatalytic performance. The theoretical calculation of electronic structures for pure TiO_2 and Co-doped TiO_2 were calculated by Density Functional Theory (DFT), which provides guidance toward understanding the variation of photocatalytic properties. The electronic calculation presented in Fig. S10 illustrated that pure TiO_2 and Co-doped TiO_2 present indirect gaps. In order to obtain more insight into the band gap narrowing for the Co-doped TiO_2 compared with TiO_2, we further investigated their total and projected partial densities of states (DOS). For TiO_2 (Fig. 7a), the states at the valence band (VB) maximum are composed of O 2p and the states at the conduction band (CB) minimum are composed of Ti 3d. Whereas, the states at the VB maximum of Co-doped TiO_2 (Fig. 7b) are composed of O 2p, Co 3d, and the states at the CB minimum are composed of Ti 3d, Co 3d, O 2p. It is clear that doping of Co species in TiO_2 will change both the VB and CB of TiO_2, and narrow the band gap of the TiO_2, thus leading to an enhanced photocatalytic performance in visible region. Moreover, the doped Co^{2+} ions (Co-O) in the surface of TiO_2 and the Co_3O_4 would enhance the water oxidation, due to their partially similar constitution (Co 3d and O 2p) in VB.[46-49, 71] Generally, O_2 is difficult to be detected in CO_2 photoreduction, due to the incidental O_2 reduction. However, in this study, we can detect the O_2 in CO_2 reduction over Co-doped TiO_2.

Therefore, the doping of Co species in TiO_2 probably increases the ability for water oxidation of TiO_2.

What are the reasons for the selective CO_2 conversion on Co-doped TiO_2 materials? A lot of properties, including the reduction potential, electronic structure, the level of conduction band and valence band of a semiconductor, should be taken into consideration. Firstly, the relative positions of the VB maximum of the samples were investigated by comparing their VB X-ray photoelectron spectroscopy (XPS) spectra. As show in Fig. S11, the VB maximum of Co-OMT-1, Co-OMT-4, Co-OMT-6 and Co-OMT-7 are, respectively, 0.19, 1.06, 1.32 and 1.38 eV higher than that of pure TiO_2. Furthermore, the Fermi level and CB can be roughly estimated by flat band potential obtained from the Mott-Schottky plots (Fig. S12). On the basis of the Fermi levels, valence band of XPS, and band gaps, the potentials of VB and CB of the samples could be drawn in the Fig. 7c. The potential at the bottom of the conduction band of Co-doped TiO_2 is higher than that at the bottom of the conduction band of TiO_2. This may be due to the ionic radius of Co^{2+} (65 pm) is bigger than the ionic radius of Ti^{4+} (60.5 pm), which would lead to the varying octahedral ligand field in TiO_2. Then, a resulting stress in the distortion of lattice contributes to the lifting of Fermi energy and the energy of the bottom of the conduction band.[72] The results of Mott-Schottky plots in Fig. S12 prove the lifting of the Fermi level of TiO_2 after doping Co, which is consistent with the previous reports.[73-75] It is observable from Fig. 7c that the CB minimum of pure TiO_2 and Co-doped TiO_2 are negative enough to reach the reduction potential of CO_2 to

produce CO ($CO_2 + 2H^+ + 2e^- \rightarrow CO + H_2O$, -0.07 V vs. NHE at pH=0) or CH_4 ($CO_2 + 8H^+ + 8e^- \rightarrow CH_4 + 2H_2O$, 0.17 V vs. NHE at pH=0). It is worth noting that pure TiO_2 and Co-doped TiO_2, also can reduce H_2O to H_2 ($2H^+ + 2e^- \rightarrow H_2$, 0 V vs. NHE at pH=0), which compete with CO_2 reduction, while the Co_3O_4 is only able to reduce CO_2 to CH_4. However, as the doped content of cobalt (Co^{2+}) increases, it will promote the formation of oxygen vacancies, as shown in UV-vis absorption spectra (500–700 nm).[76] As we know, electron spin resonance (ESR) measurement is a common technique to detect the spin polarized charge state of defective TiO_2 nanostructures.[77-79] In order to further prove the existence and increase of oxygen vacancies in Co-doped TiO_2, we have supplemented the ESR experiments of the samples and showed the signal induced by oxygen vacancies. As shown in Figure 7d, Co_3O_4 and undoped TiO_2 show no signals except the signals of Mn^{2+} which are used as the reference, while the symmetrical ESR peaks with g=2.002 was observed, which can be assigned to single-electron-trapped oxygen vacancy.[80,81] It was found that, the concentration of single-electron-trapped oxygen vacancy of Co-doped TiO_2 increased with the content of doping Co. This implies that doping Co into TiO_2 would promote the forming the oxygen vacancy in TiO_2, agreed with the literatures.[54,82] According to the Tanc plots (Fig. S6b), we deduced that the levels of oxygen vacancies are near around -0.05 V (vs. NHE at pH=0) for Co-OMT-6 and Co-OMT-7, which cannot reduce CO_2 to CO, as shown in Fig. 7c. In these cases, some excited electrons would transfer to the levels of oxygen vacancies

16

from CB, which only reduce CO_2 to CH_4. Thus, it is promising to improve the selective production of CH_4 by introducing cobalt species into TiO_2.

4. Conclusion

In summary, we have developed a novel visible-light-driven photocatalyst based on the ordered mesoporous Co-doped TiO_2. The highly ordered mesoporous structure effectively improves the photocatalytic activity and stability, and the doping of Co species increases the visible-light absorption and the ability for water oxidation of TiO_2. The optimal molar ratio of Co/Ti is 0.025, which shows the best activity of 0.09 µmol $g^{-1} h^{-1}$ (CH_4) and 1.94 µmol $g^{-1} h^{-1}$ (CO). Furthermore, an important observation is that the selectivity of products can be controlled by adjusting the molar ratio of Co/Ti in Co-doped TiO_2. When the molar ratio of Co/Ti increases to 0.2, the generated rate of CH_4 reaches to 0.258 µmol $g^{-1} h^{-1}$, due to the formation of oxygen vacancies in Co-doped TiO_2 nanocomposites. This study opens a new strategic approach to develop the visible light active photocatalysts for selectively catalyzing CO_2 reduction.

Footnote

Electronic supplementary information (ESI) available: Additional TG/DTA, SEM images, ESR, X-ray photoelectron spectroscopy, the Tauc plots, GC-MS spectra, electronic structures, Valence band XPS spectra, and Mott-Schottky plots of the samples. See DOI:

Notes and references

1   C. Le Quéré, M. R. Raupach and J. G. Canadell, *Nat. Geosci.*, 2009, **2**, 831–836.

2   S. C. Roy, O. K. Varghese, M. Paulose and C. A. Grimes, *ACS Nano,* 2010, **4**, 1259–1278.

3   N. S. Lewis and D. G. Nocera, *P. Natl. Acad. Sci. USA.,* 2006, **103**, 15729–15735.

4   C. Graves, S. D. Ebbesen, M. Mogensen and K. S. Lackner, *Renew. Sust. Energ. Rev.*, 2011, **15**, 1–23.

5   H. Tong, S. Ouyang, Y. Bi, N. Umezawa, M. Oshikiri and J. Ye, *Adv. Mater.*, 2012, **24**, 229–251.

6   A. J. Bard and M. A. Fox, *Acc. Chem. Res.*, 1995, **28**, 141–145.

7   W. Wang, S. Wang, X. Ma and J. Gong, Recent Advances in Catalytic Hydrogenation of Carbon Dioxide. *Chem. Soc. Rev.*, 2011, **40**, 3703–3727.

8   Y. Hori, H. Wakebe, T. Tsukamoto and O. Koga, *Electrochim. Acta*, 1994, **39**, 1833–183.

9   M. Rakowski Dubois and D. L. Dubois, *Acc. Chem. Res.*, 2009, **42**, 1974–1982.

10 A. B. Muñoz-García and E. A. Carter, *J. Am. Chem. Soc.*, 2012, **134**, 13600–13603.

11 S. N. Habisreutinger, L. Schmidt-Mende and J. K. Stolarczyk, *Angew. Chem. Int. Ed.*, 2013, **52**, 7372–7408.

12 W. Tu, Y. Zhou and Z. Zou. *Adv. Mater.*, 2014, **26**, 4607–4626.

13 E. E. Barton, D. M. Rampulla and A. B. Bocarsly, *J. Am. Chem. Soc.*, 2008, **130**, 6342–6344.

14 W. C. Chueh, C. Falter, M. Abbott, D. Scipio, P. Furler, S. M. Haile and A. Steinfeld, *Science*, 2010, **330**, 1797–1801.

15 X. Meng, T. Wang, L. Liu, S. Ouyang, P. Li, H. Hu, T. Kako, H. Iwai, A. Tanaka and J. Ye. *Angew. Chem. Int. Ed.*, 2014, **53**, 11478–11482.

16 W. Tu, Y. Zhou, Q. Liu, Z. Tian, J. Gao, X. Chen, H. Zhang, J. Liu and Z. Zou, *Adv. Funct. Mater.*, 2012, **22**, 1215–1221.

17 W. Tu, Y. Zhou, Q. Liu, S. Yan, S. Bao, X. Wang, M. Xiao and Z. Zou, *Adv. Funct. Mater.*, 2012, **23**, 1743–1749.

18 X. Meng, S. Ouyang, T. Kako, P. Li, Q. Yu, T. Wang and J. Ye, *Chem. Commun.*, 2014, **50**, 11517–11519.

19 J. Yu, J. Low, W. Xiao, P. Zhou and M. Jaroniec, *J. Am. Chem. Soc.*, 2014, **136**, 8839–8842.

20   D. D. Sui, X. H. Yin, H. Z. Dong, S. Y. Qin, J. S. Chen and W. L. Jiang, *Catal. Lett.*, 2012, **142**, 1202–1210.

21   H. Zhou, J. Guo, P. Li, T. Fan, D. Zhang and J. H. Ye, *Sci. Rep.*, 2013, **3**, 1667.

22   P. Li, S. Ouyang, Y. Zhang, T. Kako and J. Ye, *J. Mater. Chem. A*, 2013, **1**, 1185–1191.

23   P. Li, H. Xu, L. Liu, T. Kako, N. Umezawa, H. Abe and J. Ye, J. *Mater. Chem. A*, 2014, **2**, 5606–5609.

24   J. W. Lekse, M. K. Underwood, J. P. Lewis and C. Matranga, *J. Phys. Chem. C*, 2012, **116**, 1865–1872.

25   S. C. Yan, S. X. Ouyang, J. Gao, M. Yang, J. Y. Feng, X. X. Fan, L. J. Wan, Z. S. Li, J. H. Ye, Y. Zhou and Z. G. Zou, *Angew. Chem. Int. Ed.*, 2010, **49**, 6400–6404.

26   S. Yan, J. Wang, H. Gao, N. Wang, H. Yu, Z. Li, Y. Zhou and Z. Zou, *Adv. Funct. Mater.*, 2013, **23**, 758–763.

27   Q. Liu, Y. Zhou, J. H. Kou, X. Y. Chen, Z. P. Tian, J. Gao, S. C. Yan and Z. G. Zou, *J. Am. Chem. Soc.*, 2010, **132**, 14385–14387.

28   S. Yan, L. Wan, Z. Li and Z. Zou, *Chem. Commun.*, 2011, **47**, 5632–5634.

29   K. Teramura, S.-i. Okuoka, H. Tsuneoka, T. Shishido and T. Tanaka, *Appl. Catal. B*, 2010, **96**, 565–568.

30 Q. Liu, Y. Zhou, Z. P. Tian, X. Y. Chen, J. Gao and Z. G. Zou, *J. Mater. Chem.*, 2012, **22**, 2033–2038.

31 N. Zhang, S. Ouyang, T. Kako and J. Ye, *Chem. Commun.*, 2012, **48**, 1269–1271.

32 Y. S. Chaudhary, T. W. Woolerton, C. S. Allen, J. H. Warner, E. Pierce, S. W. Ragsdale and F. A. Armstrong,. *Chem. Commun.*, 2012, **48**, 58–60.

33 H. Fujiwara, H. Hosokawa, K. Murakoshi, Y. Wada, S. Yanagida, T. Okada and H. Kobayashi, *J. Phys. Chem. B*, 1997, **101**, 8270–8278.

34 S. Sato, T. Arai, T. Morikawa, K. Uemura, T. M. Suzuki, H. Tanaka and T. Kajino, *J. Am. Chem. Soc.*, 2011, **133**, 15240–15243.

35 T. Arai, S. Sato, T. Kajino and T. Morikawa, *Energy Environ. Sci*., 2013, **6**, 1274–1282.

36 Y. Fu, D. Sun, Y. Chen, R. Huang, Z. Ding, X. Fu and Z. Li, *Angew. Chem. Int. Ed.*, 2012, **51**, 3364–3367.

37 C. Wang , Z. Xie, K. E. deKrafft and W. Lin, *J. Am. Chem. Soc.*, 2011, **133**, 13445–13454.

38 O. K. Varghese, M. Paulose, T. J. LaTempa and C. A. Grimes, *Nano. Lett.*, 2009, **9**, 731–737.

39 W. N. Wang, J. Park and P. Biswas, *Catal. Sci. Technol.*, 2011, **1**, 593–600.

40   Q. Y. Zhang, Y. Li, E. A. Ackerman, M. Gajdardziska-Josifovska and H. L. Li, *Appl. Catal. A*, 2011, **400**, 195–202.

41   K. Xie, N. Umezawa, N. Zhang, P. Reunchan, Y. Zhang and J. Ye, *Energy Environ. Sci.*, 2011, **4**, 4211–4219.

42   S. Sato, T. Morikawa, S. Saeki, T. Kajino and T. Motohiro, *Angew. Chem. Int. Ed.*, 2010, **49**, 5101–5105.

43   T. Wang, X. Meng, P. Li, S. Ouyang, K. Chang, G. Liu, Z. Mei and J. Ye, *Nano Energy*, 2014, **9**, 50–60.

44   W. Zhou, W. Li, J.-Q. Wang, Y. Qu, Y. Yang, Y. Xie, K. Zhang, L. Wang, H. Fu and D. Zhao, *J. Am. Chem. Soc.*, 2014, **136**, 9280–9283.

45   Y. Wang, F. Wang, Y. Chen, D. Zhang, B. Li, S. Kang, X. Li and L. Cui. *Appl. Catal. B*, 2014, **147**, 602–609.

46   A. Harriman, *Eur. J. Inorg. Chem.*, 2014, **4**, 573–580.

47   M. Zhang, M. de Respinis and H. Frei, *Nat. Chem.*, 2014, **6**, 362–367.

48   Y. Liang, Y. Li, H. Wang, J. Zhou, J. Wang, T. Regier and H. Dai, *Nat. Mater.*, 2011, **10**, 780–786.

49   L. Liao, Q. Zhang, Z. Su, Z. Zhao, Y. Wang, Y. Li, X. Lu, D. Wei, G. Feng, Q. Yu, X. Cai, J. Zhao, Z. Ren, H. Fang, F. Robles-Hernandez, S. Baldelli and J. Bao, *Nat. Nanotechnol.*, 2014, **9**, 69–73.

50 H. M. Yang, J. Ouyang and A. D. Tang, *J. Phys. Chem. B*, 2007, **111**, 8006–8013.

51 D. Barreca, A. Gasparotto, O. I. Lebedev, C. Maccato, A. Pozza, E. Tondello, S. Turner and G. V. Tendeloo, *CrystEngComm*, 2010, **12**, 2185–2197.

52 R. D. Shannon, *Acta Cryst. A*, 1976, **32**, 751–767.

53 J. D. Bryan, S. M. Heald, S. A. Chambers and D. R. Gamelin, *J. Am. Chem. Soc.*, 2004, **126**, 11640–11647.

54 V. I. Anisimov, M. A. Korotin, I. A. Nekrasov, A. S. Mylnikova, A. V. Lukoyanov, J. L. Wang and Z. Zeng, *J. Phys.: Condens. Matter*, 2006, **18**, 1695–1704.

55 J. Lin, Y. Lin, P. Liu, M. J. Meziani, L. F. Allard and Y.-P. Sun, J. Am. Chem. Soc. 2002, **124**, 11514–11518.

56 D. Gallant, M. Pezolet and S. Simard, *J. Phys. Chem. B*, 2006, **110**, 6871–6880.

57 K. S. W. Sing, D. H. Everett, R. A. W. Haul, L. Moscou, R. A. Pierotti, J. Rouquérol and T. Siemieniewska, *Pure Appl. Chem.*, 1985, **57**, 603–619.

58 W. G. Tu, Y. Zhou and Z. G. Zou, *Adv. Funct. Mater.*, 2013, **23**, 4996–5008.

59 W. Q. Fan, Q. H. Zhang and Y. Wang, *Phys. Chem. Chem. Phys.*, 2013, **15**, 2632–2649.

60 S. C. Roy, O. K. Varghese, M. Paulose and C. A. Grimes, *ACS Nano*, 2010, **4**, 1259–1278.

61 S. S. Khine Ma, K. Maeda, T. Hisatomi, M. Tabata, A. Kudo and K. Domen, *Chem. Eur. J.*, 2013, **19**, 7480–7486.

62 S. Yan, H. Yu, N. Wang, Z. Li and Z. Zou, *Chem. Commun.*, 2012, **48**, 1048–1050.

63 J. Yu, J. Jin, B. Cheng and M. Jaroniec, *J. Mater. Chem. A*, 2014, **2**, 3407–3416.

64 J. Pan, X. Wu, L. Wang, G. Liu, G. Q. Lu and H. M. Cheng, *Chem. Commun.*, 2011, **47**, 8361–8363.

65 W. Jiao, L. Wang, G. Liu, G. Q. Lu and H. M. Cheng, *ACS Catal.*, 2012, **2**, 1854–1859.

66 H. Zhou, P. Li, J. Guo, R. Yan, T. Fan, D. Zhang and J. Ye. *Nanoscales*, 2015, **7**, 113–120.

67 D. Kong, J. Ziang Y. Tan, F. Yang, J. Zeng and X. Zhang, *Appl. Surf. Sci.*, 2013, **277**, 105–110.

68 T. Ohno, T. Higo, N. Murakami, H. Saito,Q. Zhang, Y. Yang and T. Tsubot, *Appl. Catal. B*, 2014, **152–153**, 309–316.

69 M. Tahir, and N. S. Amin, *Appl. Catal. B*, 2015, **162**, 98–109.

70 Q. Li, L. Zong, C. Li and J. Yang. *Appl. Surf. Sci.*, 2014, **314**, 458–463.

71 Y. Meng, D. Gu, F. Zhang, Y. Shi, H. Yang, Z. Li, C. Yu, B. Tu and D. Zhao, *Angew. Chem. Int. Ed.*, 2005, **44**, 7053–7059.

72 J. Y. Shi, W. H. Leng, W. C. Zhu, J. Q. Zhang, C. N. Cao. *Chem. Eng. Technol.*, 2006, **29**, 146−154.

73 Q. Xiao, G.-Z. Qiu and Y.-H. Hu, *Chin. J. Nonferrous Met.*, 2001, **11**, 900–904.

74 J. Y. Shi, W. H. Leng, X. F. Cheng, Z. ZHANG, J.-Q. Zhang and C.-N. CAO, *Chin. J. Nonferrous Met.*, 2007, **17**, 1536–1542.

75 T.-H. Wang, Y.-X. Li, S.-Q. PENG, G.-X. Lv and S.-B. Li, Acta Chim. Sinica. 2005, **63**, 797-801.

76 M. D. Segall, J. D. L. Philip, M. J. Probert, C. J. Pickard, P. J. Hasnip, S. J. Clark and M. C. Payne, *J. Phys. Condens. Matter*, 2002, **14**, 2717–2744.

77 C. D. Valentin, G. Pacchioni, A. Selloni , S. Livraghi and E. Giamello, *J. Phys. Chem. B*, 2005, **109**, 11414–11419.

78 C. P. Kumar, N. O. Gopal, T. C. Wang, M.-S. Wong and S. C. Ke, *J. Phys. Chem. B*, 2006, **110**, 5223-5229.

79 B. Santara, P. K. Giri, K. Imakita and M. Fujii, *J. Phys. Chem. C,* 2013, **117**, 23402–23411.

80 E. Serwicka, *Colloids Surf.*, 1985, **13**, 287–293.

81 J. Zhang, Z. Jin, C. Feng, L. Yu, J. Zhang and Z. Zhang, *J. Solid State Chem.*, 2001, **184**, 3066-3073.

82 H. Weng, X. Yang, J. Dong, H. Mizuseki, M. Kawasaki and Y. Kawazoe, *Phys. Rev. B*, 2004, **69**, 125219.
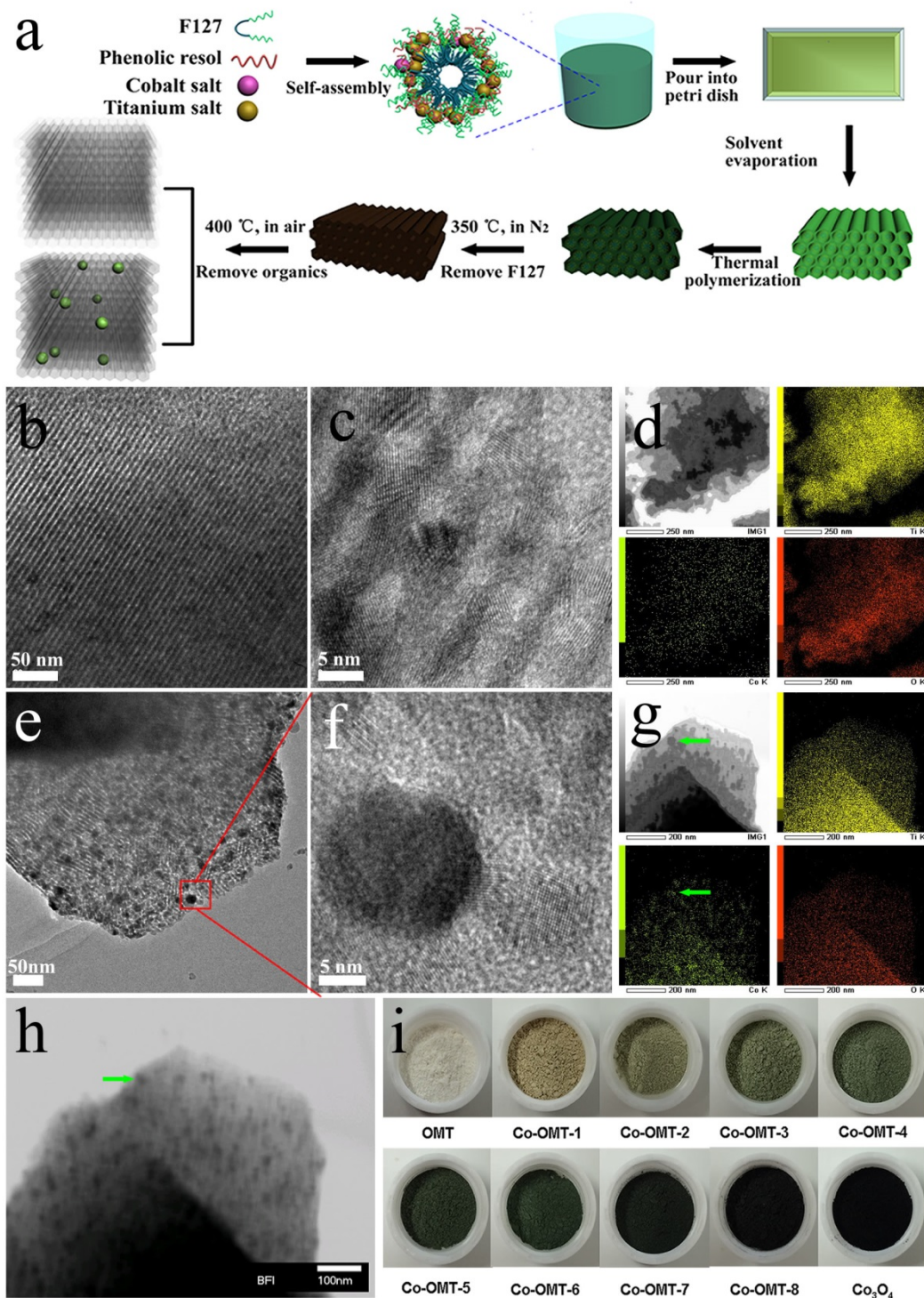
Fig. 1 (a) Schematic illustration of the formation process of ordered mesoporous Co-doped TiO₂. TEM images and elemental maping images of (b,c,d) Co-OMT-1 and (e,f,g) Co-OMT-7. (h) STEM image of Co-OMT-7. (i) The photos of the samples.
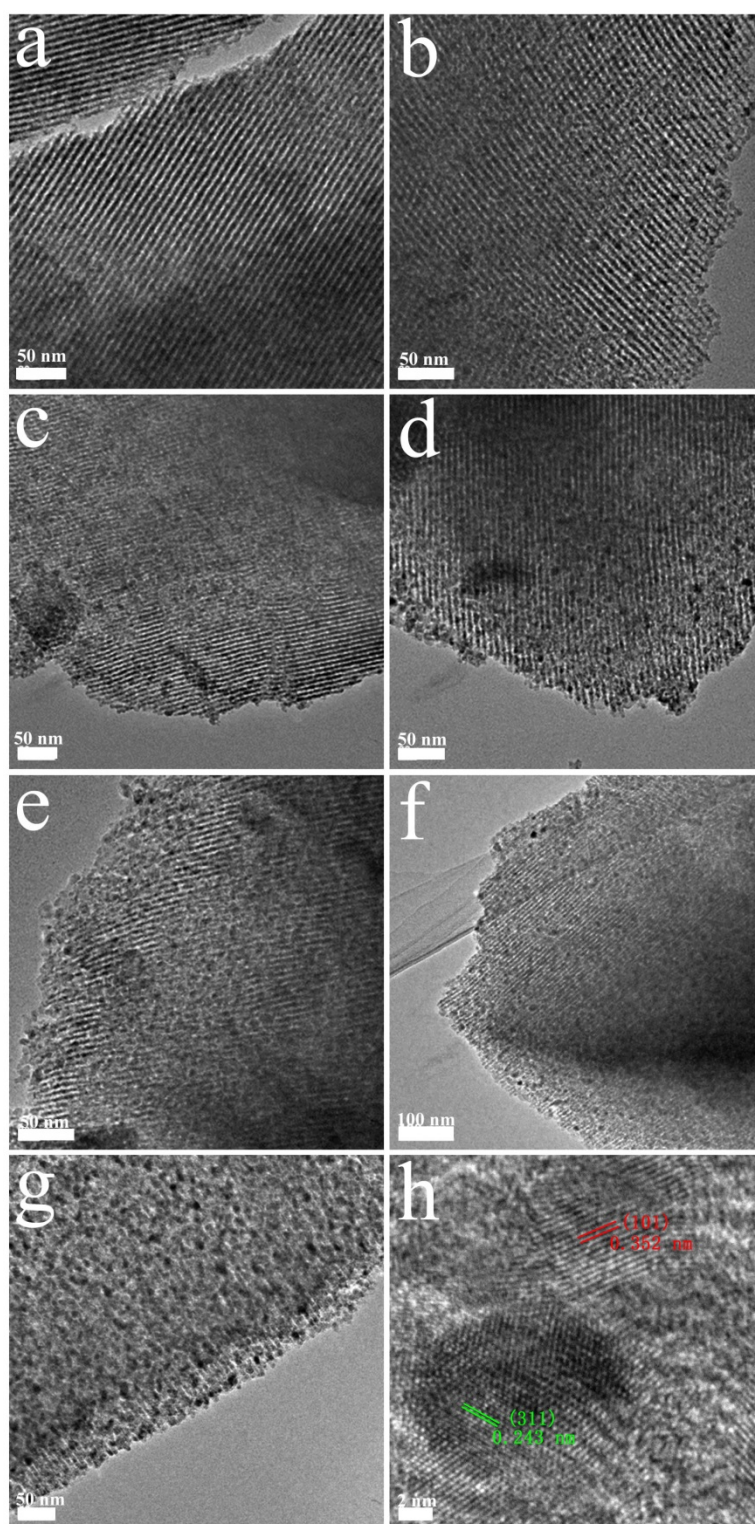
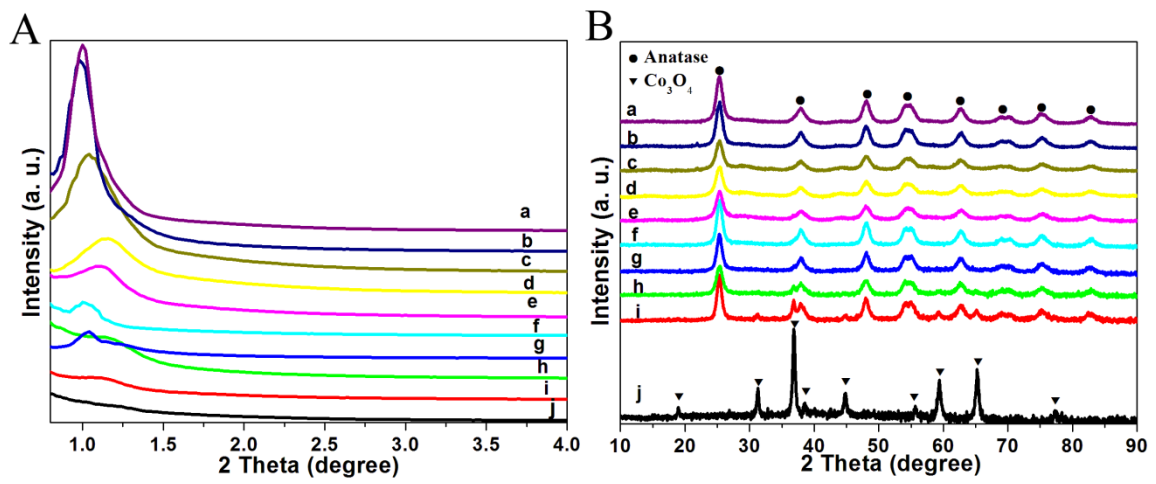**Fig. 2** TEM images of (a) OMT, (b) Co-OMT-2, (c) Co-OMT-3, (d) Co-OMT-4, (e) Co-OMT-5 (f) Co-OMT-6 and (g,h) Co-OMT-8.

Fig. 3 (A) Small-angle XRD and (B) wide-angle XRD patterns of the samples: (a) OMT, (b) Co-OMT-1, (c) Co-OMT-2, (d) Co-OMT-3, (e) Co-OMT-4, (f) Co-OMT-5, (g) Co-OMT-6, (h) Co-OMT-7, (i) Co-OMT-8, (j) Co_3O_4.
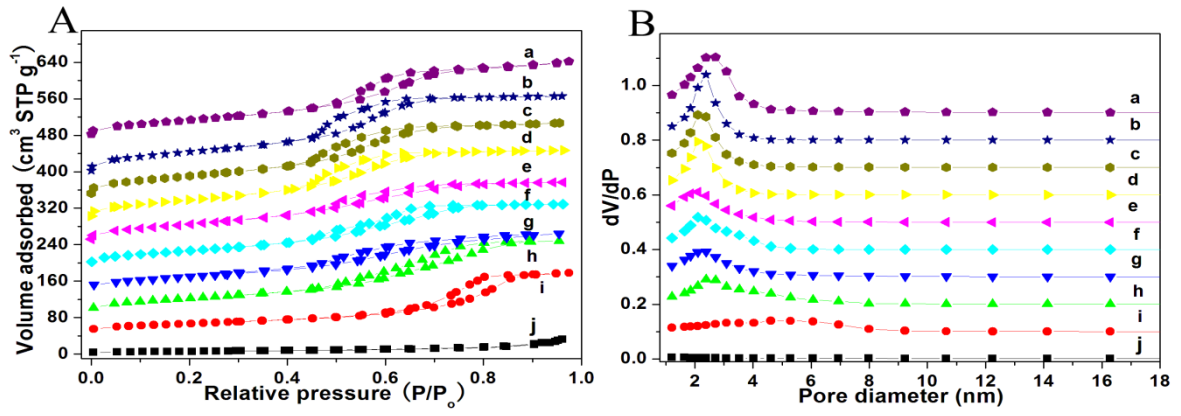
Fig. 4 (A) N$_2$ adsorption-desorption isotherms and (B) pore size distribution of the samples: (a) OMT, (b) Co-OMT-1, (c) Co-OMT-2, (d) Co-OMT-3, (e) Co-OMT-4, (f) Co-OMT-5, (g) Co-OMT-6, (h) Co-OMT-7, (i) Co-OMT-8, (j) Co$_3$O$_4$.
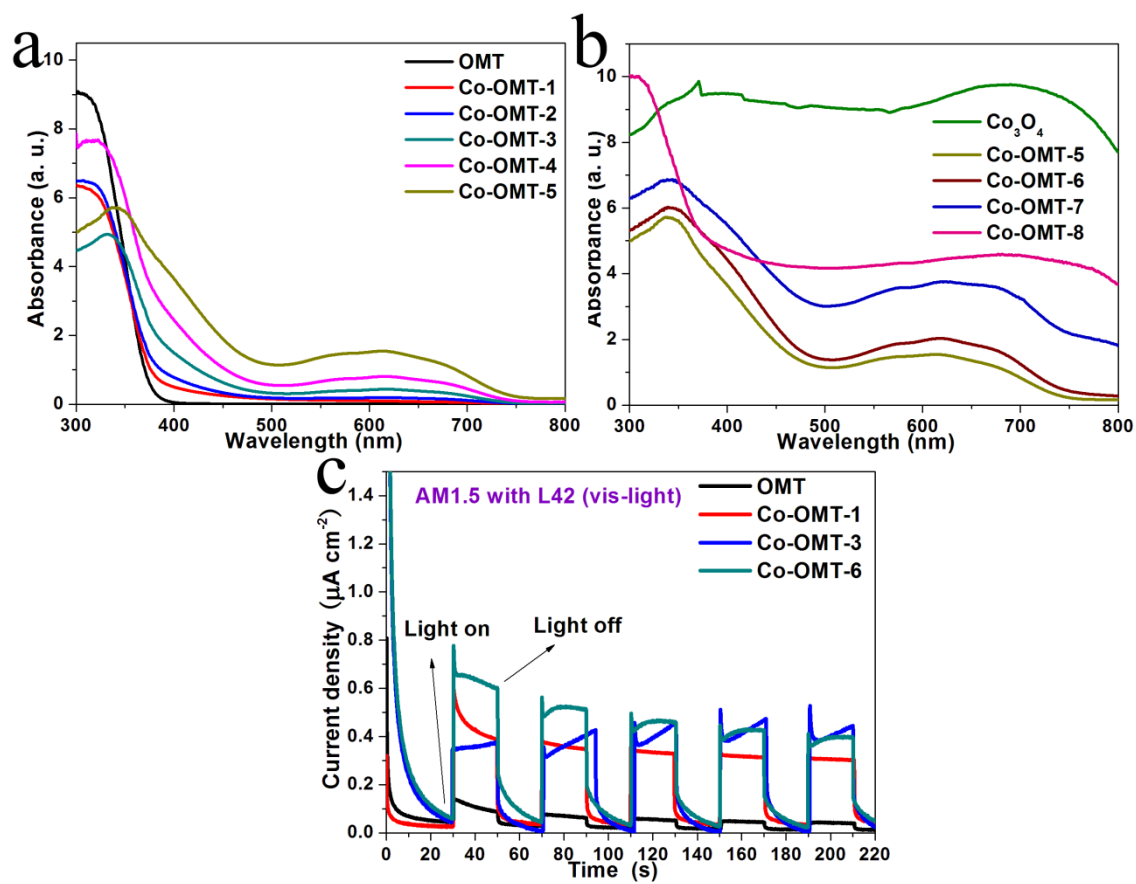
Fig. 5 (a,b) UV-vis absorption spectra and (c) photocurrent response in 0.5 M Na$_2$SO$_4$ solution at 0.4 V (vs. Ag/AgCl) of the samples.
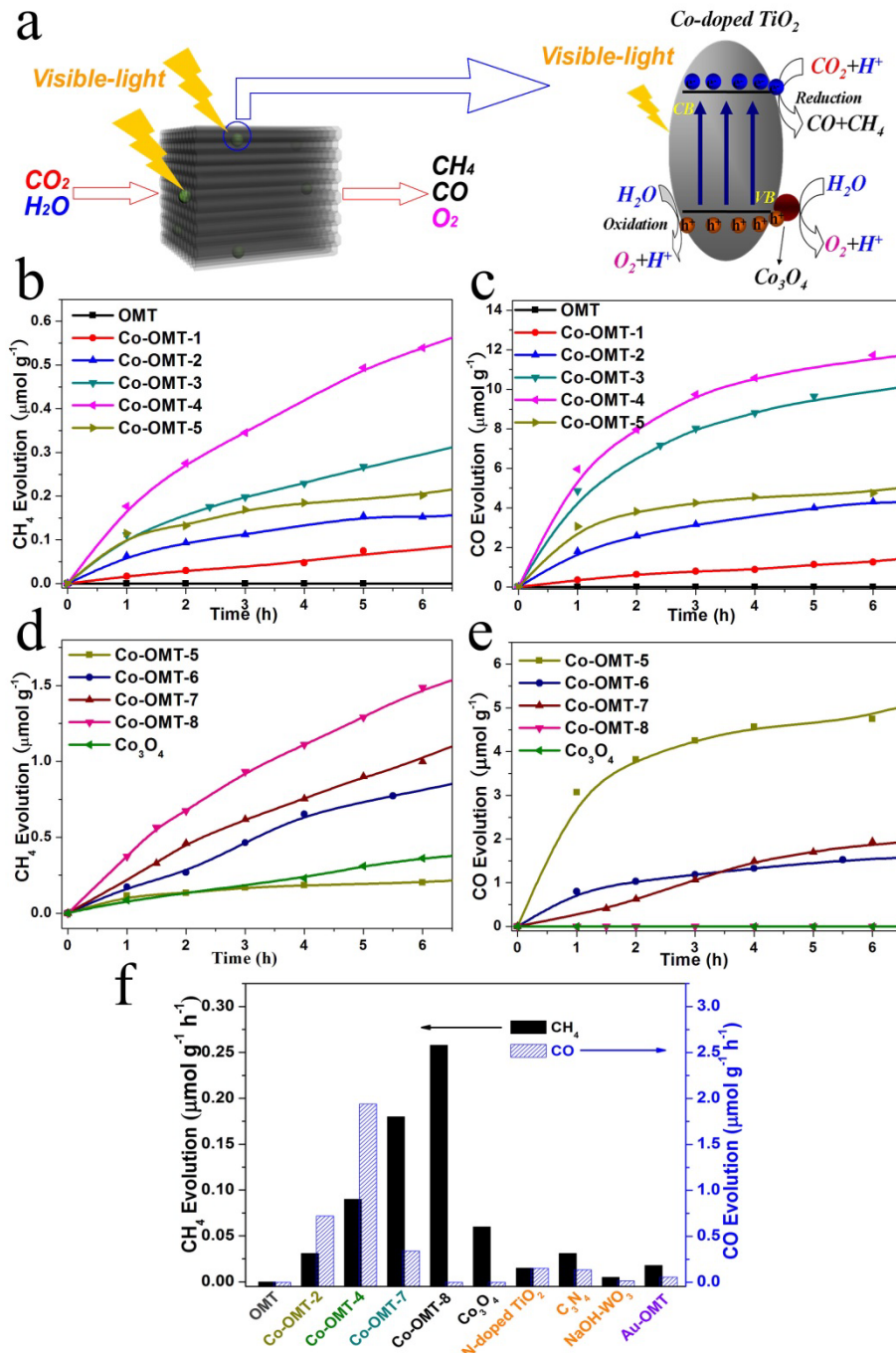
Fig. 6 (a) Schematic illustration of basic mechanism of TiO_2 photocatalyic process. CH_4 (b,d) and CO (c,e) evolution over various samples under visible light. (f) Comparison of photocatalytic activity of the samples with common photocatalysts under visible light, calculated according to the mounts evolved in 6 h.
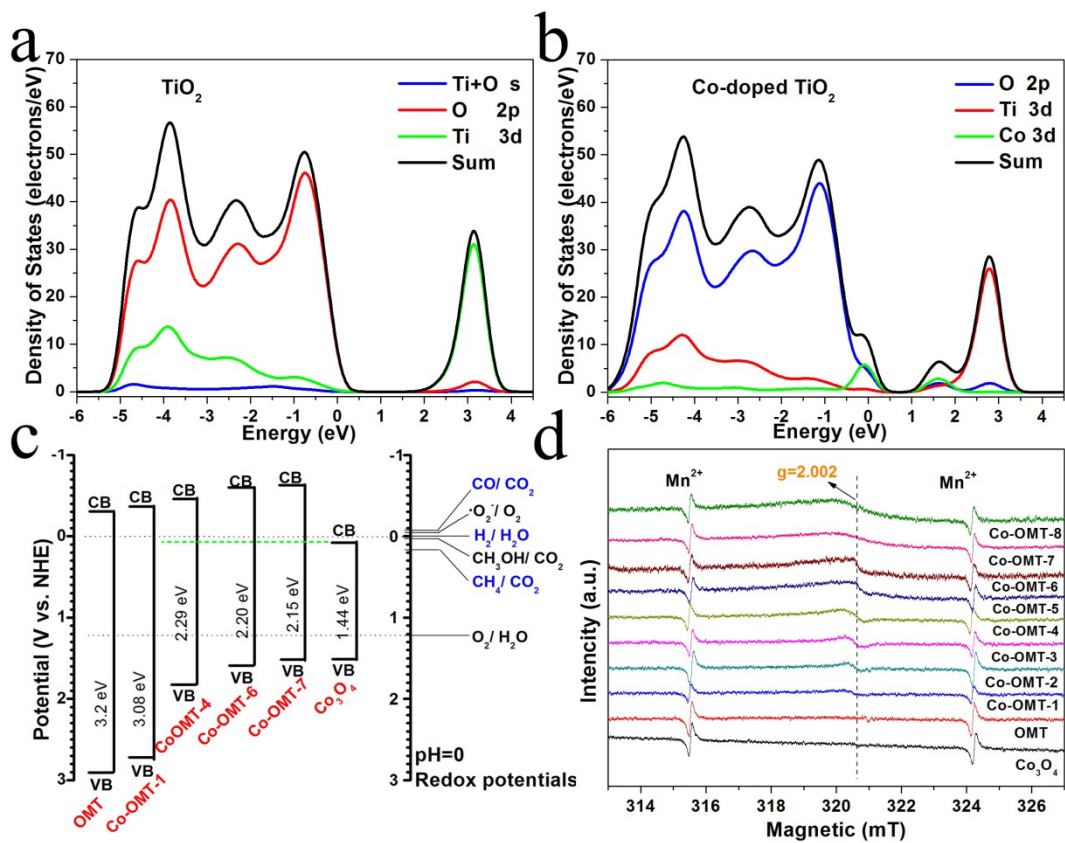
Fig. 7 DOS of (a) anatase TiO_2 and (b) $Co_xTi_{1-x}O_2$ (x=0.0625). (c) schematic illustration of the band structures of the samples. (d) ESR spectra of the samples, and Mn^{2+} is used as position correction.

Table 1 Molar ratio and structural parameters of the samples.

Sample	Molar ratio (Co:Ti)	S_{BET} (m^2 g^{-1}) [a]	V_{total} (cm^3 g^{-1}) [b]	P (nm) [c]
OMT	0	246	0.31	2.7
Co-OMT-1	0.002	231	0.29	2.4
Co-OMT-2	0.005	222	0.27	2.1
Co-OMT-3	0.01	214	0.26	2.1
Co-OMT-4	0.025	201	0.23	2.1
Co-OMT-5	0.05	173	0.23	2.1
Co-OMT-6	0.1	148	0.21	2.4
Co-OMT-7	0.15	154	0.26	2.4
Co-OMT-8	0.2	97	0.21	4.6
Co_3O_4	-	20	0.05	-

[a] S_{BET} is calculated by BET equation; [b] V_{total} (pore volume) is calculated at p/p_0=0.950~0.995; [c] Peak of pore size (P) is calculated by BJH method.

Table 2 Activities and selectivities of the samples.

Sample	Molar ratio (Co：Ti)	S_{BET} ($m^2 g^{-1}$)	Band gap (eV)	Products ($\mu mol\ g^{-1}\ h^{-1}$)				
				CH_4	CO	$CH_4/(CH_4+CO)$	H_2	O_2
OMT	0	246	3.20	0	0	-	0	0
Co-OMT-1	0.002	231	3.08	0.015	0.23	6.1%	trace	trace
Co-OMT-2	0.005	222	3.01	0.031	0.72	4.1%	0.052	0.128
Co-OMT-3	0.01	214	2.32	0.053	1.64	3.1%	0.54	0.156
Co-OMT-4	0.025	201	2.29	0.090	1.94	4.4%	0.74	0.133
Co-OMT-5	0.05	173	2.21	0.046	0.79	5.5%	1.89	0.119
Co-OMT-6	0.1	154	2.20	0.140	0.33	29.8%	0.45	0.108
Co-OMT-7	0.15	148	2.15	0.180	0.34	34.6%	0.029	0.072
Co-OMT-8	0.2	97	2.19	0.258	0	100%	0	0.140
Co_3O_4	-	20	1.44	0.060	0	100%	0	0.071